

## Long-range electron-electron interactions in quantum dot systems and applications in quantum chemistry

Knörzer, J.; Van Diepen, C. J.; Hsiao, T. K.; Giedke, G.; Mukhopadhyay, U.; Reichl, C.; Wegscheider, W.; Cirac, J. I.; Vandersypen, L. M.K.

**DOI**

[10.1103/PhysRevResearch.4.033043](https://doi.org/10.1103/PhysRevResearch.4.033043)

**Publication date**

2022

**Document Version**

Final published version

**Published in**

Physical Review Research

**Citation (APA)**

Knörzer, J., Van Diepen, C. J., Hsiao, T. K., Giedke, G., Mukhopadhyay, U., Reichl, C., Wegscheider, W., Cirac, J. I., & Vandersypen, L. M. K. (2022). Long-range electron-electron interactions in quantum dot systems and applications in quantum chemistry. *Physical Review Research*, 4(3), Article 033043. <https://doi.org/10.1103/PhysRevResearch.4.033043>

**Important note**

To cite this publication, please use the final published version (if applicable).  
Please check the document version above.

**Copyright**

Other than for strictly personal use, it is not permitted to download, forward or distribute the text or part of it, without the consent of the author(s) and/or copyright holder(s), unless the work is under an open content license such as Creative Commons.

**Takedown policy**

Please contact us and provide details if you believe this document breaches copyrights.  
We will remove access to the work immediately and investigate your claim.

# Long-range electron-electron interactions in quantum dot systems and applications in quantum chemistry

J. Knörzer<sup>1,2,\*</sup>, C. J. van Diepen<sup>3,‡</sup>, T.-K. Hsiao<sup>3</sup>, G. Giedke<sup>4,5</sup>, U. Mukhopadhyay<sup>3</sup>,  
C. Reichl<sup>6</sup>, W. Wegscheider<sup>6</sup>, J. I. Cirac<sup>1,2,§</sup> and L. M. K. Vandersypen<sup>3,||</sup>

<sup>1</sup>Max-Planck-Institut für Quantenoptik, Hans-Kopfermann-Strasse 1, 85748 Garching, Germany


<sup>2</sup>Munich Center for Quantum Science and Technology, Schellingstrasse 4, 80799 München, Germany

<sup>3</sup>QuTech and Kavli Institute of Nanoscience, Delft University of Technology, 2600 GA Delft, Netherlands

<sup>4</sup>Donostia International Physics Center, Paseo Manuel de Lardizabal 4, E-20018 San Sebastián, Spain

<sup>5</sup>Ikerbasque Foundation for Science, Maria Diaz de Haro 3, E-48013 Bilbao, Spain

<sup>6</sup>Solid State Physics Laboratory, ETH Zürich, 8093 Zürich, Switzerland

 (Received 17 February 2022; revised 25 February 2022; accepted 15 June 2022; published 15 July 2022)

Long-range interactions play a key role in several phenomena of quantum physics and chemistry. To study these phenomena, analog quantum simulators provide an appealing alternative to classical numerical methods. Gate-defined quantum dots have been established as a platform for quantum simulation, but for those experiments the effect of long-range interactions between the electrons did not play a crucial role. Here we present a detailed experimental characterization of long-range electron-electron interactions in an array of gate-defined semiconductor quantum dots. We demonstrate significant interaction strength among electrons that are separated by up to four sites, and show that our theoretical prediction of the screening effects matches well the experimental results. Based on these findings, we investigate how long-range interactions in quantum dot arrays may be utilized for analog simulations of artificial quantum matter. We numerically show that about ten quantum dots are sufficient to observe binding for a one-dimensional H<sub>2</sub>-like molecule. These combined experimental and theoretical results pave the way for future quantum simulations with quantum dot arrays and benchmarks of numerical methods in quantum chemistry.

DOI: [10.1103/PhysRevResearch.4.033043](https://doi.org/10.1103/PhysRevResearch.4.033043)

## I. INTRODUCTION

Electromagnetic forces between electrons play a crucial role in quantum physics and chemistry. They are a key ingredient for many phenomena, ranging from molecular binding [1], Wigner crystallization [2], and exciton formation [3] to high-temperature superconductivity [4]. While their exact treatment in quantum many-body systems remains numerically challenging, analog quantum simulators [5,6] offer an alternative setting for the study of complex quantum systems with long-range interactions. Yet in most physical systems, particles interact locally or at short distances only. It is therefore of great interest to investigate experimental platforms in which long-range interactions between charged particles occur naturally.

Electrons confined to semiconductor quantum dots (QDs) provide a versatile test bed for analog quantum simulation of Fermi-Hubbard physics [6–8]. Previous experimental studies have addressed the transition from Coulomb blockade to collective Coulomb blockade [9], itinerant ferromagnetism when doping with a single hole [10], and Heisenberg magnetism arising in the Mott-insulator regime [11]. However, long-range electron-electron interactions have not yet been capitalized on in gate-defined QD systems, and their effect was previously either tuned away or remained as an unwanted disturbance. The character of the electron-electron interaction is also relevant for the operation of spin qubits in QD arrays with shared control lines [12].

Transport measurements on double quantum dots (DQDs) more than two decades ago [13] already revealed interactions between electrons on neighboring sites. In more recent work, these interactions have been used to induce entanglement between spin qubits in separate DQDs [14]. Interactions between electrons separated by multiple sites have been studied to assess the readout performance [15] and the tunability of the interaction between DQD qubits [16] and to induce a cascade of electrons enabling distant spin readout [17]. However, a detailed study of electron-electron interactions as a function of distance has not yet been performed. While such a characterization is technically challenging as it requires a high degree of control over the potential landscape of a sufficiently large system, recent achievements in tuning and controlling multidot arrays [18–21] facilitate the

\*These authors contributed equally to this work.

†Present address: Institute for Theoretical Studies, ETH Zürich, 8093 Zürich, Switzerland.

‡Present address: Niels Bohr Institute, University of Copenhagen, Copenhagen, Denmark.

§ignacio.cirac@mpq.mpg.de

||l.m.k.vandersypen@tudelft.nl

Published by the American Physical Society under the terms of the [Creative Commons Attribution 4.0 International](https://creativecommons.org/licenses/by/4.0/) license. Further distribution of this work must maintain attribution to the author(s) and the published article's title, journal citation, and DOI. Open access publication funded by the Max Planck Society.

formation of increasingly large and homogeneously coupled QD arrays.

In this paper, we present a detailed examination of long-range electrostatic interactions between electrons confined to a semiconductor QD system. In our paper we operate a six-site QD array with homogeneous tunnel coupling and two charge sensors. We record a charge-stability diagram for each dot-dot pair in the array, thus explicitly accounting for non-nearest-neighbor interactions. From the analysis of these diagrams we extract the electron-electron interaction potential as a function of distance, which is shown and discussed in Sec. II. We detect interactions between electrons that are up to four sites away from each other. Furthermore, we model the interaction numerically, taking screening effects due to metallic gates into account, and find good agreement between experiment and theory. As a promising application of our findings, we discuss prospects for analog simulations of low-dimensional, artificial atoms and molecules in Sec. III, that may help to benchmark and improve existing numerical methods in quantum chemistry (QC). Inspired by the ideas outlined in a recent proposal for neutral atoms in optical lattices [22], we start from the tight-binding description of our QD system and regard it as a linear discretization of an artificial atom, or molecule. We calculate the low-lying eigenstates of the tight-binding model and discuss their relation to the simulated chemical systems. Based on our numerical results, we project that QD arrays with approximately ten sites are sufficient for proof-of-principle simulations of molecular dissociation, which is within reach of state-of-the-art experiments. We also discuss relevant experimental techniques for the implementation of QC with QD arrays. Finally, in Sec. IV, we summarize our findings and give perspectives for future work.

## II. CHARACTERIZATION OF INTERACTION POTENTIAL

In this section, we introduce the experimental system and its theoretical model, which is employed in the later analysis. Subsequently we present the experimental characterization of on-site and intersite interactions in the QD array, and show that these agree well with results from numerical calculations.

### A. Device

The QD system consists of a linear array of six QDs and two charge sensors, and is formed in a GaAs/AlGaAs heterostructure. Figure 1(a) shows a scanning electron micrograph of the active region of a device similar to the one used in this experiment, which is designed for up to eight QDs with two charge sensors and has previously been operated as a Heisenberg spin chain [11]. At the GaAs/AlGaAs interface, 90 nm below the surface and 40 nm below a silicon doping layer, a two-dimensional electron gas forms. The potential landscape at the interface is shaped by applying voltages on the gates, which are patterned at the surface with a dot spacing  $a_{\text{QD}} = 160$  nm. The device is cooled in a dilution refrigerator, which results in an electron reservoir temperature of about 100 mK (roughly 10  $\mu\text{eV}$ ).

### B. Tight-binding model

To characterize the interaction potential between electrons, we start from a tight-binding description and consider the

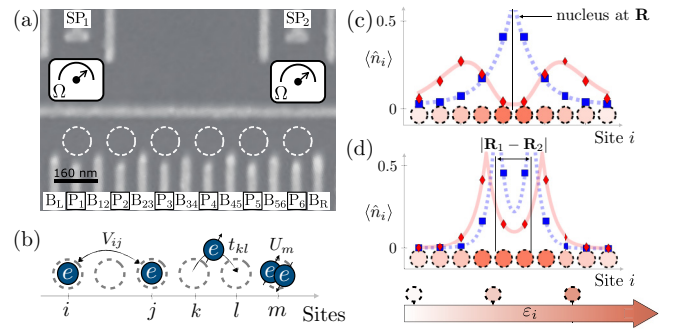


FIG. 1. Quantum dot system with schematics of chemistry simulations. (a) Scanning electron micrograph of the device. Dot locations are indicated with dashed circles, and charge sensors are indicated by resistance meters labeled with  $\Omega$ . Barrier gates between sites  $i$  and  $j$  are labeled by  $B_{ij}$ , and plunger gates at site  $k$  are labeled by  $P_k$ . Charge sensors are controlled by gates  $SP_1$  and  $SP_2$ , respectively. (b) Sketch of competing terms in Eq. (1) describing the quantum dot array: intersite interaction  $V_{ij}$ , tunnel coupling  $t_{kl}$ , and on-site interaction  $U_m$ . (c) Schematic of the QD array and its relation to atomic QC simulation, exemplarily shown for ten QDs. The electron-nucleus interaction potential of an artificial hydrogen atom is encoded in the local energy offsets  $\varepsilon_i$ . (d) Similar setup in the case of the molecular ion  $H_2^+$  with two nuclei at  $\mathbf{R}_1$  and  $\mathbf{R}_2$ , respectively. The system can be studied for different internuclear distances  $|\mathbf{R}_1 - \mathbf{R}_2|$  separately. Blue squares (red diamonds) indicate the local expectation values  $\langle n_i \rangle$  in the ground state (first-excited state), and the blue-dashed (red-solid) line shows the fit to the ground-state (excited-state) wave function [23,24]. The orange colorscale encodes the local potential offset.

single-band extended Fermi-Hubbard model [9,25,26]

$$H = \underbrace{\sum_i U_i n_{i\uparrow} n_{i\downarrow}}_{=:H_{ee}} + \underbrace{\sum_{i \neq j} V_{ij} n_i n_j}_{=:H_{ne}} - \underbrace{\sum_{\langle i,j \rangle, \sigma} t_{ij} c_{i\sigma}^\dagger c_{j\sigma}}_{=:H_{kin}}, \quad (1)$$

where the dot occupation at site  $i$  is denoted by  $n_i = n_{i\uparrow} + n_{i\downarrow}$  and  $n_{i\sigma} = c_{i\sigma}^\dagger c_{i\sigma}$  with the annihilation (creation) operator  $c_{i\sigma}^{(\dagger)}$  for an electron with spin  $\sigma$ . The last sum is restricted to nearest-neighbor hopping only, as indicated by  $\langle \cdot, \cdot \rangle$ .  $t_{ij}$  denotes the tunnel coupling between sites  $i$  and  $j$ ,  $\varepsilon_i$  the local energy offset,  $U_i$  the on-site interaction, and  $V_{ij}$  the intersite interaction strength [see also Fig. 1(b)]. The local energy offsets,  $\varepsilon_i$ , and the tunnel couplings,  $t_{ij}$ , can be tuned with the gate voltages, and thus can be adjusted to the problem under study. The Hamiltonian consists of a contribution from electronic interactions ( $H_{ee}$ ), potential ( $H_{ne}$ ), and electron hopping ( $H_{kin}$ ). This notation will prove useful for the discussion in Sec. III.

### C. Experimental results

The interaction potential is characterized based on a set of charge-stability diagrams. This set contains a diagram for each dot and a diagram for each pair of dots. Before

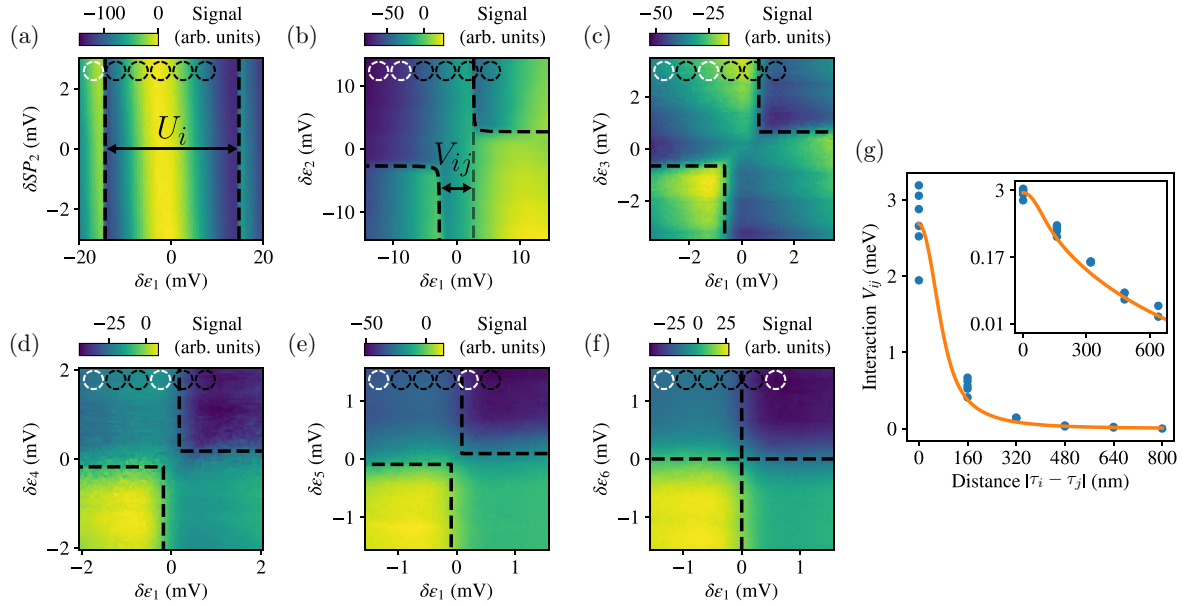


FIG. 2. [(a)–(f)] Charge-stability diagrams showing the sum of signals from both charge sensors as a function of the local energy offsets for the dots highlighted by the white dashed circles. (a) For the leftmost dot only the left sensor signal is shown, and is measured relative to the gate for the rightmost sensor. This gate here acts as a dummy, because it has negligible effect on both the leftmost dot and the signal from the left sensor. The broad vertical band is a Coulomb peak for the left sensor, which appears due to crosstalk from  $\epsilon_1$ . (b–f) For the leftmost dot in combination with a dot (b) one, (c) two, (d) three, (e) four, and (f) five sites away. Black dashed lines are fits to the anticrossings, and are used to extract the interaction elements; the lighter dashed line in (b) is a guide to the eye to indicate the voltage of the shifted vertical addition line. The voltages are converted to energies with the lever arms  $\{105, 94, 104, 86, 104, 95\} \mu\text{eV mV}^{-1}$ , which were obtained with photon-assisted tunneling experiments [27]. (g) Interaction matrix elements  $V_{ij}$  vs distance between QDs  $i$  and  $j$ , which are centered around  $\tau_i$  and  $\tau_j$ , respectively. Blue dots indicate the experimentally obtained interaction elements and the solid line shows the numerical result based on screening due to the gate metal as described in detail in Appendix B. The uncertainties in the interaction elements are dominated by uncertainties in the lever arms, estimated to be below 10%, and the electron temperature ( $\approx 10 \mu\text{eV}$ ). The inset shows the interaction and fits on a logarithmic scale for better comparison. For simplicity  $U_i$  is denoted as  $V_{ii}$ .

the diagrams are measured, the voltages are tuned to the center of the charge region with one electron per dot and homogeneous nearest-neighbor tunnel couplings,  $t \approx 20 \mu\text{eV}$ . From that configuration, for each diagram only the chemical potentials for the respective dots are temporarily changed. For the pairwise diagrams the respective chemical potentials are, in addition, offset to center at an anticrossing where a charge is added on one dot in the pair and removed from the other. The diagrams involving the leftmost dot are shown in Figs. 2(a)–2(f). The full set of pairwise diagrams, which for six QDs consists of 15 diagrams, is shown in Fig. 4. This set of diagrams can explicitly reveal crosstalk for the control of chemical potentials, thus also for non-nearest-neighbor sites. Here this crosstalk has already been compensated for with virtual gates [9,18,19,28].

The on-site interaction elements,  $U_i$ , are obtained from the separation between the addition lines for the first and second electron on the respective dot [see Fig. 2(a)]. The intersite interaction elements,  $V_{ij}$ , are extracted by modeling the anticrossings in the charge-stability diagrams with [9]

$$\delta\epsilon_i + \delta\epsilon_j = \pm [V_{ij} + \sqrt{(\delta\epsilon_i - \delta\epsilon_j)^2 + 4t_{ij}^2}], \quad (2)$$

with  $\delta\epsilon_i = \epsilon_i - \epsilon_{i,0}$  where  $\epsilon_{i,0}$  is the local energy offset at the center of the respective anticrossing. The anticrossing model is converted into a two-dimensional patch, which is fitted onto

the charge-stability diagrams [see Figs. 2(b)–2(f)], using an edge detection algorithm [29]. Figure 2(g) shows all values for  $U_i$  and  $V_{ij}$  as extracted from the full set of diagrams. The interaction strength shows a clear decay with distance, and is significant up to a distance of four sites. The spread in interaction values for a fixed distance is explained by residual disorder in the potential landscape, which most noticeably affects the on-site interaction as it strongly depends on size and shape of the QD confinement. A comparison of the intersite interaction values between the left and right sides of QDs 2–5 did not reveal asymmetries, which indicates that the QDs are centered around the intended locations.

#### D. Numerical results

The dominant source for screening of the interaction is the metal of the gates above the QDs [see Fig. 1(a)]. Other sources could contribute to screening, such as the surrounding two-dimensional electron gas, dopants, and impurities, but are expected to be less important due to the device geometry or a relatively low density of mobile charge carriers. The electrons on the QDs themselves are not expected to contribute to screening much because they are rather strongly confined to their respective QDs and were kept deep in the Coulomb blockade regime for the characterization of the interaction potential. Based on this assumption, the depth of the interface,



and the gate pattern, we numerically calculate the screened interaction between two electrons as a function of distance. It can be evaluated from the charge distribution induced in the metallic surface layer [30]. The underlying numerical approach is summarized in Appendix B. We compare the numerical results with the experimental results by using a least-squares fit and observe good agreement. In our calculations, we account for the finite dot size using a Gaussian basis set to describe the electronic wave functions, which yields a decay of  $V_{ij}$  as shown in Fig. 2(g). The fitted dot size is mainly determined by the measurement results of local (on-site) interactions,  $U_i$ , which together with the numerical approach outlined in Appendix B result in an accurate model for the nonlocal (intersite) interaction  $V_{ij}$ . Most notably we find that the electron-electron interaction potential  $V_{ee}$  decays polynomially with distance. At large distance, our prediction is consistent with a fitted subexponential (power-law) decay  $V_{ee}(|\mathbf{r} - \mathbf{r}'|) \sim C/|\mathbf{r} - \mathbf{r}'|^\alpha$  where  $\alpha \lesssim 3$ . This finding is in agreement with an analytical estimate, based on the image-charge method, for a device of which the surface is completely covered by metal and the fact that the present device is only partially covered by metallic gates (see Appendix B). That estimate yields a cubic decay of interactions with distance, i.e.,  $\alpha = 3$ , and more closely describes accumulation-mode devices with a multilayer gate stack, such as those based on silicon and germanium [15,31].

### III. APPLICATIONS IN QUANTUM CHEMISTRY

In Sec. II, we have shown that electrons in the QD array interact at long distances via a screened Coulomb repulsion. In the following, we study how this insight may be utilized in future experiments for the analog simulation of artificial atoms and molecules.

#### A. Theoretical framework

A major task in QC is to study the low-energy physics of systems with  $N_e$  electrons and  $N_c$  nuclei. Within the usually employed Born-Oppenheimer approximation, the positions of the nuclei are fixed at  $\mathbf{R}_1, \dots, \mathbf{R}_{N_c}$ , and the total Hamiltonian can be decomposed as  $H_{QC} = H_{\text{kin}} + H_{ee} + H_{ne}$  with a kinetic part and electron-electron and nucleus-electron interactions, respectively. Here we consider a discretized instance of this problem, that can be simulated using a QD array with  $N$  sites (see Fig. 1). We investigate a one-dimensional array as in Sec. II, but we note that the upcoming theoretical analysis can be extended to two-dimensional lattices.

We start from the model in Eq. (1) with a homogeneous tunnel coupling  $t$ . The kinetic term  $H_{\text{kin}}$  describes electrons hopping at a rate  $t$ , that are confined to an electrostatic potential landscape. With the choice for the energy offsets

$$\varepsilon_i = \sum_{k=1}^{N_c} V_{ne}(|\tau_i - \mathbf{R}_k|), \quad (3)$$

we interpret  $H_{ne}$  from Eq. (1) as an analog of the attractive nucleus-electron interaction in QC, where  $\tau_i$  denotes the location of the  $i$ th dot. In the QD array, the form of the interaction potential  $V_{ne}$  may be adjusted by an adequate choice of chemical potentials. For example,  $\varepsilon_i = V_0/|\tau_i - \mathbf{R}|$  may be chosen

to mirror the Coulomb law in the presence of a single nucleus at position  $\mathbf{R}$ , with an interaction strength  $V_0$ . Finally, the electron-electron interaction is captured by  $H_{ee}$  and has been characterized in Sec. II. It is dictated by the actual interaction potential between charge carriers in the semiconductor. While the exact form of  $V_{ee}$  [see Eq. (B1)] differs from the behavior of electrons in natural systems, it still permits long-distance interactions and allows for the simulation of artificial multielectron atoms and molecules. It is partly the presence of such long-range interactions that poses serious computational challenges in the numerical treatment of quantum matter, e.g., in molecular simulations.

Upon this reinterpretation of terms in the Fermi-Hubbard model (1), the physical parameters of the QD array can be associated with the characteristic length and energy scales of the QC Hamiltonian. In atomic physics, the effective Bohr radius  $a_0$  relates the kinetic and potential energy scales. In our system, these are characterized by nearest-neighbor hopping,  $t$ , and nearest-neighbor Coulomb interaction,  $V_0/a_{\text{QD}}$ , respectively. This enables us to identify  $a_0 = t/(V_0/a_{\text{QD}})$  and thus to introduce [32]

$$\eta \equiv \frac{a_0}{a_{\text{QD}}} = \frac{t}{V_0}, \quad \text{Ry} = \frac{V_0^2}{t} = \eta^{-2}t, \quad (4)$$

with the Rydberg energy  $\text{Ry}$ . The ratio  $\eta$  in Eq. (4) determines the discretization error introduced by the finite array and relates to how well the continuum limit can be recovered. In particular, (i) at too small  $\eta$  the atomic orbitals cannot be well resolved, as for this the effective Bohr radius should span several QD sites, and (ii) too large  $\eta$  implies that the simulated atom or molecule does not fit into the array.

#### B. Numerical results

In the following we demonstrate that relatively small QD arrays can be used to study basic properties of simple artificial atoms and molecules. For this aim, we calculate the low-energy eigenstates of the tight-binding Hamiltonian [see Eq. (1)] for realistic system parameters and discuss finite-size effects.

*Atoms.* First we study an artificial hydrogen atom by setting  $\varepsilon_i = V_0/|\tau_i - \mathbf{R}|$  to define a single nucleus located at  $\mathbf{R}$  in the center of the array [see Fig. 1(c)]. We calculate the low-energy spectrum of the system described by  $H$  in Eq. (1), and relate the eigenenergy  $E$  to an atomic binding energy  $E_b = E + 2t$ . At a fixed tunnel coupling  $t$ ,  $V_0 = t/\eta$  needs to be optimized in order to approximate the continuum limit well. With system size,  $N$ , sufficiently large, the Balmer-like series  $E_n = -\text{Ry}/n^2$  of a one-dimensional hydrogen atom [23] is reproduced if  $\eta$  is neither too small nor too large. Importantly, it can be seen that even relatively small arrays resolve quantized energy levels at intermediate  $\eta$  and approximately yield the analytical result of the continuum case [see Figs. 3(a) and 3(b)]. As comparison see Fig. 3(c) for a very large  $N = 300$ , where the energy plateaus coincide with the analytical result over a relatively wide range of  $\eta$ . Signatures of this behavior can already be observed at much smaller  $N$ , which shows that basic atomic properties can be studied using currently available setups with approximately ten dots. The probability density of the one-dimensional hy-

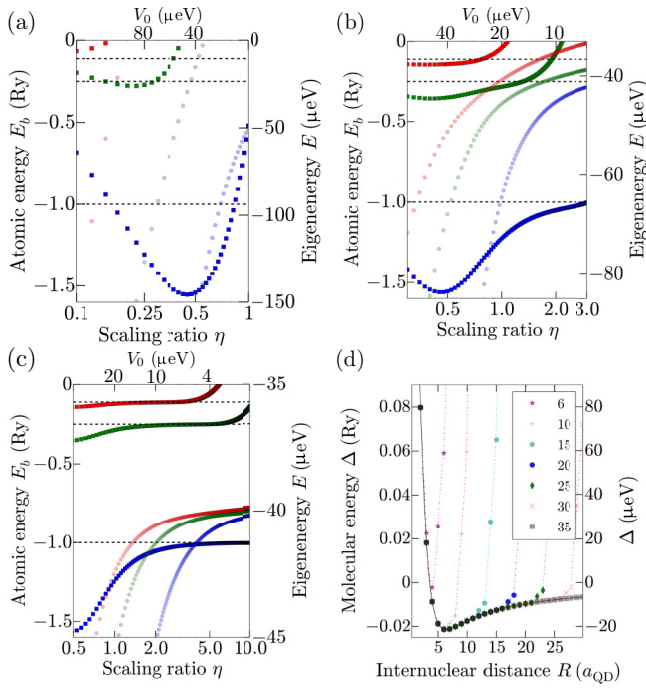


FIG. 3. Numerical results for the atom and the two-electron molecule. Lowest part of the artificial hydrogenlike atom spectrum as a function of  $V_0$  and  $\eta = t/V_0$  for system sizes (a)  $N = 6$ , (b)  $N = 25$ , and (c)  $N = 300$ . The left axis (dark squares) shows the atomic binding energy  $E_b$  in Ry, while the right axis (light circles) shows the corresponding eigenenergies of Eq. (1) in  $\mu\text{eV}$ . Shown are the ground (blue), first-excited-state (green), and second-excited-state (red) energies. The dashed lines indicate the three lowest Balmer series values. In all cases,  $t = 20 \mu\text{eV}$ . (d) Molecular binding energy  $\Delta$  (see text) for the artificial  $H_2$ -like molecule with two electrons interacting via effective potential  $V_{ee}$ , and two nuclei separated by distance  $R$ . Shown is the molecular binding energy for different system sizes  $N = 6, 10, 15, \dots, 35$ . Curve fits to guide the eye (solid line for  $N = 35$  and dash-dotted lines for all other  $N$ ). Other parameters:  $t = 40 \mu\text{eV}$ ,  $V_0 = 200 \mu\text{eV}$ , and  $\text{Ry} = 1 \text{ meV}$ .

drogen atom is directly related to the ground- and excited-state occupation numbers  $\langle \hat{n}_i \rangle$ , as depicted in Fig. 1(c).

**Molecules.** Next we demonstrate the simulator's ability to uncover essential molecular properties. For this aim we consider a system composed of two electrons and two nuclei. In order to obtain the dissociation curve of this artificial  $H_2$ -like molecule, we calculate the low-energy spectrum of  $H + V_{nn}$ , where  $V_{nn}$  denotes the nucleus-nucleus interaction potential. The electron-electron interaction is governed by the screened interaction in the semiconductor, while for the electron-nucleus and nucleus-nucleus interactions we consider a Coulomb potential, i.e.,  $V_{nn} = V_0/R$ . The internuclear distance  $R$  can be varied by adjusting the local offsets  $\varepsilon_i$ . Within the Born-Oppenheimer approximation, the positions of the nuclei are considered to be fixed, and thus the term  $V_{nn}$  is simply added to the measurement result  $\langle H \rangle$  in the end.

We note that the interaction potential  $V_{ee}$  is device specific and cannot be altered *in situ*. Given a suitable gate pattern, the interaction matrix elements  $V_{ij}$ , the local energy offsets  $\varepsilon_i$ , and nearest-neighbor hopping  $t_{ij}$  may in principle still be tuned

independently from one another [33]. For simplicity, we fix  $t$  and  $V_0$  in our numerical simulation and treat them as constant for all distances  $R$ . Despite the fact that, in this way, we do not optimize the scaling parameter  $\eta$  for each  $R$  separately, we obtain a molecular binding curve with a pronounced minimum as shown in Fig. 3(d). We show the molecular binding energy  $\Delta = E_{2e^-} - 2E_{e^-}$ , and thus compare the ground-state energies of the two-electron ( $E_{2e^-}$ ) and single-electron ( $E_{e^-}$ ) systems. The results show that basic molecular properties can be resolved with arrays of moderate size, e.g.,  $N \approx 10$  dots suffice for determining the bond length of the artificial molecule.

### C. Relevant experimental techniques

For the experimental implementation it is important to consider methods for the initialization of the QC simulator and the measurement of relevant system parameters. The initialization requires the QD array to be occupied with the desired total number of charges. For small systems this can be achieved based on the fact that the long-range electron-electron interaction strength is larger than the reservoir temperature. For a larger number of sites with only few charges, control over the tunnel coupling to the reservoirs can allow for first loading the desired number of charges and then isolating the QD array by raising the respective tunnel barriers [34,35].

For measurements of the simulator there are various techniques available for gate-defined QDs. The energy splittings for the artificial atom and molecule (see Fig. 3) are found to be in the 5-60  $\mu\text{eV}$  range, and thus can be probed with microwave spectroscopy such as used for the observation of covalent bonding on a DQD [36]. The microwave excitation and charge sensor detection require a change in charge distribution between ground and excited state, which are shown in Figs. 1(c) and 1(d) for the atom and molecular ion, respectively. In addition, a tilt on local offsets  $\varepsilon_i$  could be applied (see Appendix C), which has a similar effect as an electric field that induces a dc Stark shift for an atom or molecule. Applying a tilt can be used to map out a trend in the energy splitting, which could be used to determine the splitting at conditions, e.g., zero tilt, where no change in charge distribution is induced. This concept has been used for instance to extract interdot tunnel couplings [36]. For the QC simulator a tilt could in particular prove useful for the simulation of molecules with larger internuclear separation (see Fig. 6). In addition, the transition probabilities can be increased by applying the microwave signal on multiple gates. Another useful technique for QDs is gate-based reflectometry by which the electrical susceptibility can be measured [37–40]. This offers an alternative to obtaining the energy splitting at conditions where no change in charge distribution is induced, but the quantum capacitance is nonzero.

Complimentary measurements of the energy levels of the QC simulator, for example, for the ground state of the two-electron molecule shown in Fig. 3(d), could be performed by using a well-defined reference level, e.g., the reservoir Fermi level or another QD. The energy level of the QC simulator can then be extracted by identifying for which global shift the simulator level is on resonance with the reference level. In this way, the energy levels can be compared for different scaling ratios,  $\eta$ , and different internuclear distances. Combined with

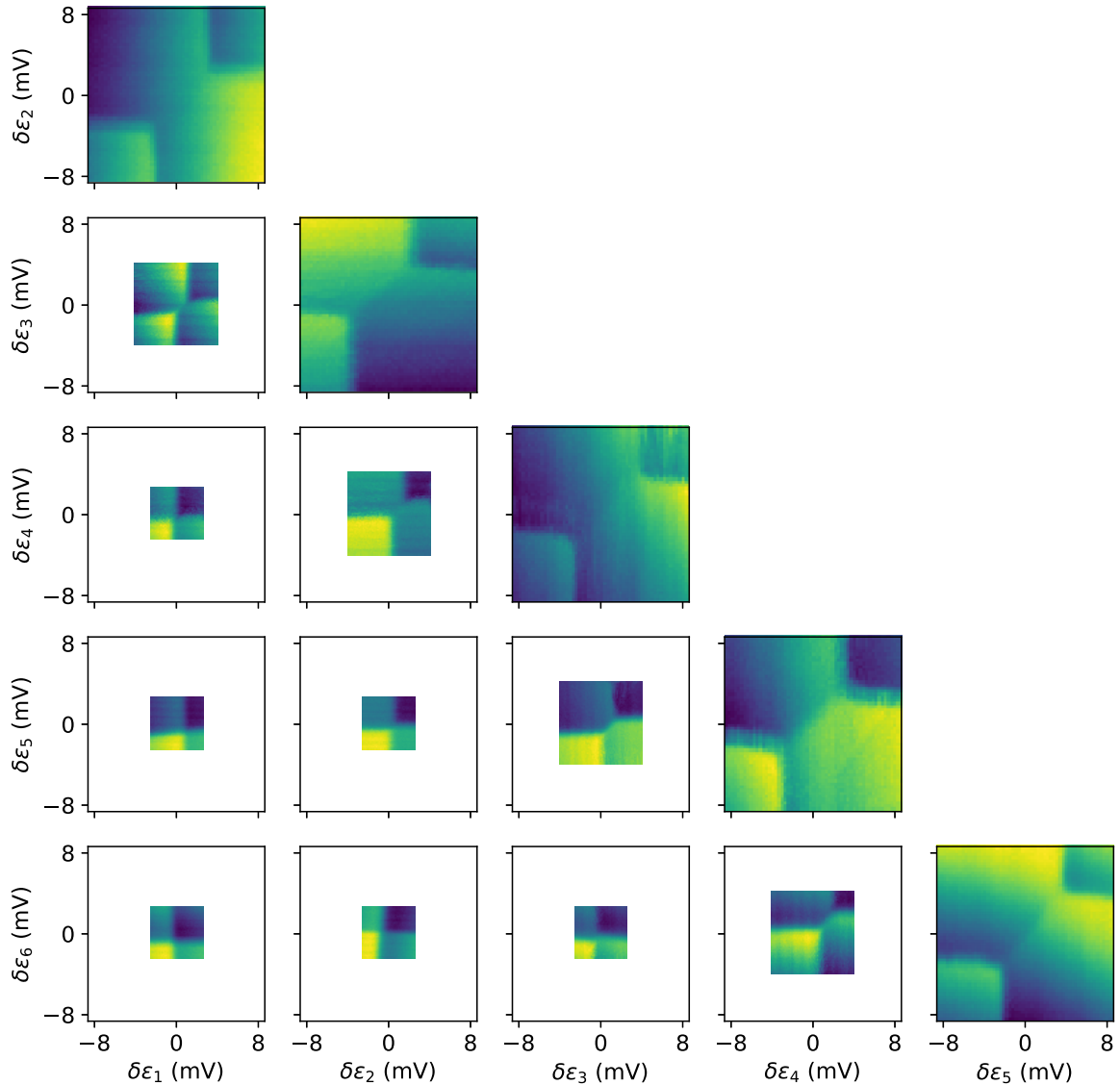


FIG. 4. Full set of pairwise charge-stability diagrams. The leftmost column shows the diagrams presented in Fig. 2 in the main text. For non-nearest-neighbor pairs smaller voltage ranges were used to maintain sufficient resolution with the same number of data points.

microwave spectroscopy the energy spectrum can then be mapped out experimentally in a way similar to the numerical results shown in Fig. 3.

#### IV. CONCLUSIONS AND OUTLOOK

In summary, we have experimentally characterized the long-range electron-electron interactions in a gate-defined quantum dot array. The interactions were experimentally found to be detectable between electrons up to four sites away. We compared a toy model of the electrostatic interaction that considers metallic gates as the main screening source and found good agreement with our measurement results. In future work it will be instructive to analyze in more detail how the form of long-range interaction potentials can be controlled by an adequate choice of gate patterns.

We have also discussed how quantum dot systems may be utilized for future analog simulations of artificial quantum matter, both in single-electron systems and in many-electron

systems with long-range interactions. Using numerical simulations, we demonstrated that quantized atomic binding energies can be resolved and that the interactions are sufficiently strong to explore nontrivial properties like molecular dissociation curves. We have shown that proof-of-principle demonstrations may already be performed using state-of-the-art experimental setups of approximately ten quantum dots. Hence our paper opens up the path for future quantum simulation experiments and studies of artificial atoms and molecules using semiconductor quantum dot arrays. Due to the computationally challenging problems that arise in the context of quantum chemistry, this may prove beneficial for the benchmarking of existing numerical techniques and development of new theoretical methods. In addition, these well-controlled quantum systems with long-range interactions are also promising for future investigations of other debated phenomena, such as Wigner crystallization [41,42], exciton formation [3], high-temperature superconductivity [4,7], and the nature of many-body excited states [43,44]. On a different

note, similar ideas to the ones discussed in this paper may be explored in other suitable semiconductor systems such as transition-metal dichalcogenides (TMDs) where screening is significantly reduced. While these two-dimensional materials have intriguing optoelectronic properties [45] that may offer new optical readout schemes, creating well-defined and high-quality trapping potentials for charge carriers in TMDs using gate-defined quantum dots [46] or strain fields [47] is an active topic of research.

The data reported in this paper and scripts to generate the figures are available in [48].

### ACKNOWLEDGMENTS

J.K. and J.I.C. acknowledge support from the Deutsche Forschungsgemeinschaft under Germany's Excellence Strategy (EXC-2111 Grant No. 390814868) and from European Research Council (ERC) Advanced Grant QUENOCOA under the European Union Horizon 2020 program (Grant No. 742102). G.G. acknowledges support by the Spanish AEI through Project No. PID2020-115406GB-I00 "GEQCO" and the European FET-OPEN project SPRING (Grant No. 863098). L.M.K.V. acknowledges support from an ERC Advanced Grant (QuDoFH Grant No. 882848). C.R. and W.W. acknowledge support from the Swiss National Science Foundation.

### APPENDIX A: FULL SET OF CHARGE-STABILITY DIAGRAMS

In the main text, only the charge-stability diagrams involving the leftmost dot are provided. The full set of pairwise charge-stability diagrams is shown in Fig. 4.

### APPENDIX B: SCREENED INTERACTION POTENTIAL

In this Appendix, we summarize our theoretical analysis to estimate the interaction strength as a function of distance, as depicted in Fig. 2 of the main text. The main task is to derive a form of the interaction potential  $V_{ee}$ . Given that potential, the matrix elements  $V_{ij}$  and  $U_i = V_{ii}$  can be obtained within a Wannier basis  $\{\phi_i\}_{i=1,\dots,N}$  as

$$V_{ij} = \int d^2\mathbf{r} \int d^2\mathbf{r}' |\phi_i(\mathbf{r})|^2 V_{ee}(\mathbf{r}, \mathbf{r}') |\phi_j(\mathbf{r}')|^2, \quad (\text{B1})$$

where  $V_{ee}$  denotes the two-body interaction potential between electrons. These elements can be checked for self-consistency by comparison with the tunnel coupling elements given by

$$t_{ij} = \int d^2\mathbf{r} \phi_i^*(\mathbf{r}) \left[ -\frac{\hbar^2}{2m} \nabla^2 + V(\mathbf{r}) \right] \phi_j(\mathbf{r}). \quad (\text{B2})$$

The basis states  $\phi_i$  are constructed from Gaussians centered around the central locations of the QDs, denoted by  $\tau_i$ .

#### 1. Method of image charges

We consider screening due to metallic gates as the dominant screening source in our sample. For a conservative estimate, we first calculate the screened Coulomb potential under the assumption that the whole surface layer was covered

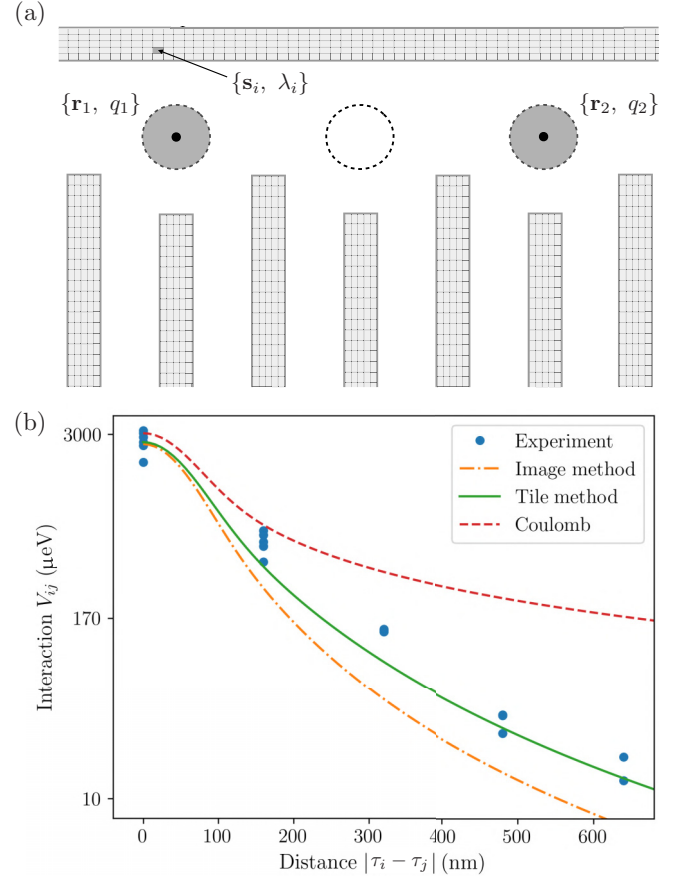


FIG. 5. Screened interaction potential. (a) Schematic illustration of the numerical procedure to calculate the screened interaction potential. The device geometry shown in Fig. 2 is taken and its surface area discretized. The interaction potential is obtained from the pairwise interaction terms of all tile charges  $\lambda_i$  at position  $\mathbf{s}_i$  and the two electrons at  $\mathbf{r}_1$  and  $\mathbf{r}_2$ . (b) Interaction matrix elements  $V_{ij}$ , between dots located at  $\tau_i$  and  $\tau_j$ , compared for different cases: unscreened Coulomb interactions (red, dashed), screened interactions via image-charge method for a surface completely covered by metal (orange, dash-dotted), and screened interaction via numerical discretization of real device geometry (green, solid).

by metal. Using the method of image charges, the screened interaction between two electrons at  $\mathbf{r}_1 = (x_1, y_1, -d)$  and  $\mathbf{r}_2 = (x_2, y_2, -d)$  takes the form

$$f_{\text{im}}(\mathbf{r}_1, \mathbf{r}_2) = 1 - \frac{\sqrt{(x_1 - x_2)^2 + (y_1 - y_2)^2}}{\sqrt{(x_1 - x_2)^2 + (y_1 - y_2)^2 + 4d^2}},$$

$$V_{ee}^{\text{im}}(\mathbf{r}_1, \mathbf{r}_2) = f_{\text{im}}(\mathbf{r}_1, \mathbf{r}_2) \frac{k_0 e^2}{|\mathbf{r}_1 - \mathbf{r}_2|}$$

$$\xrightarrow{d/|\mathbf{r}_1 - \mathbf{r}_2| \rightarrow 0} \frac{2k_0 (ed)^2}{|\mathbf{r}_1 - \mathbf{r}_2|^3}, \quad (\text{B3})$$

with  $k_0 = 1/(4\pi\epsilon\epsilon_0)$ . In our numerical simulations we use  $\epsilon = 12.9$ , the relative dielectric constant for GaAs. As Fig. 5(b) shows, this ansatz overestimates the screening effect as expected. In our sample, the surface area is only partially covered by thin metallic gates. In the following section, we calculate the screened potential due to the gates in the real device geometry.



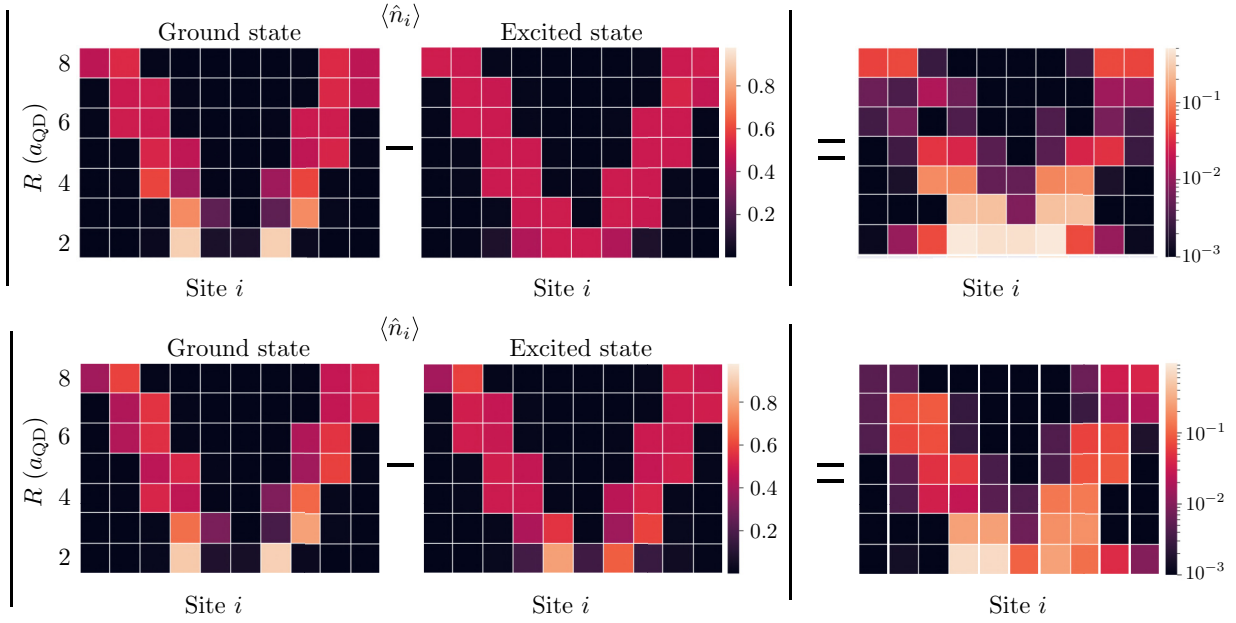


FIG. 6. Charge occupation numbers  $\langle \hat{n}_i \rangle$  for a system with  $N = 10$  QDs and two electrons. Upper panel: Results for ground (left) and first-excited (middle) state, respectively. The  $x$  axis denotes the site index of the  $i$ th dot in the array, and the  $y$  axis denotes the internuclear separation  $R/a_{\text{QD}}$ . The absolute value of the difference between the first two columns is shown on the right. Lower panel: Same as upper panel, but for a model with an additional bias term  $\Delta \varepsilon_i = (i - x_c) \times 10 \mu\text{eV}$ , where  $x_c$  denotes the center of the QD array.

## 2. Charge-tiling method

To calculate the metal-induced screening numerically, we start from the real device geometry and discretize its surface area into  $m$  tile charges  $\lambda_i (i = 1, \dots, m)$  centered around positions  $\mathbf{s}_i$  [see Fig. 5(a)]. We derive the interaction  $V_{ee}(\mathbf{r}_1, \mathbf{r}_2)$  for two electrons located  $d = 90$  nm below the surface at  $\mathbf{r}_1$  and  $\mathbf{r}_2$ , respectively. Here,  $\{\lambda_i\}_{i=1,\dots,m}$  refers to the induced tile charges due to the presence of these two electrons. With the electron charge  $q_1 = q_2 = -e$ , we obtain the electrostatic potential at tile  $i$  as

$$\tilde{V}(\mathbf{s}_i) = \sum_{k=1,2} \frac{-k_0 e}{|\mathbf{s}_i - \mathbf{r}_k|} + \sum_{j \neq i} \frac{k_0 \lambda_j}{|\mathbf{s}_j - \mathbf{s}_i|}. \quad (\text{B4})$$

We assume charge conservation in the metallic layer,  $\sum_i \lambda_i = 0$ , and a constant potential,  $\tilde{V}(\mathbf{s}_i) = \tilde{V}(\mathbf{s}_j)$ ,  $\forall i, j$ . This yields a system of linear equations that can be solved to determine the tile charges  $\lambda_i$ . Finally, the screened interaction potential energy can be obtained from

$$V_{ee}(\mathbf{r}_1, \mathbf{r}_2) = \frac{-e}{2} \sum_{k=1,2} \sum_{i=1}^m \frac{k_0 \lambda_i}{|\mathbf{r}_k - \mathbf{s}_i|} + \frac{k_0 e^2}{|\mathbf{r}_1 - \mathbf{r}_2|}. \quad (\text{B5})$$

The first term of the right-hand side of Eq. (B5) shows that the tile charges screen the bare Coulomb interaction  $\sim 1/|\mathbf{r}_1 - \mathbf{r}_2|$ . This is demonstrated in Fig. 5(b). The numerically obtained results lie between the bare Coulomb and fully screened [based on Eq. (B3)] curves. They are in good agreement with the measurement outcomes and demonstrate the long-range character of  $V_{ee}$ . We note that the size of the quantum dots, as described by the full width at half maximum of the functions  $\phi_i$ , is a fitting parameter in our numerical approach. We find this size to be  $\approx 45$  nm.

## APPENDIX C: CHARGE OCCUPATION NUMBERS

The expectation values  $\langle \hat{n}_i \rangle$  describe the spread of the electronic wave function over the QD array (see Fig. 1). As described in the main text in Sec. III C, resonant microwave excitations may be employed for probing transitions from ground to low-lying excited states. In Fig. 6 we show  $\langle \hat{n}_i \rangle$  for an artificial two-electron molecule, both for the ground and first-excited states. As shown in the figure, the difference in local occupation between ground and excited state may be enhanced by applying a potential bias, e.g., in the form of  $\varepsilon_i \propto i$ .

- 
- [1] R. H. French, V. A. Parsegian, R. Podgornik, R. F. Rajter, A. Jagota, J. Luo, D. Asthagiri, M. K. Chaudhury, Y. M. Chiang, S. Granick *et al.*, Long range interactions in nanoscale science, *Rev. Mod. Phys.* **82**, 1887 (2010).
  - [2] E. Wigner, On the interaction of electrons in metals, *Phys. Rev.* **46**, 1002 (1934).
  - [3] J. Frenkel, On the transformation of light into heat in solids. I, *Phys. Rev.* **37**, 17 (1931).
  - [4] P. W. Anderson, Twenty-five years of high-temperature superconductivity – A personal review, *J. Phys.: Conf. Ser.* **449**, 012001 (2013).
  - [5] J. I. Cirac and P. Zoller, Goals and opportunities in quantum simulation, *Nat. Phys.* **8**, 264 (2012).
  - [6] I. M. Georgescu, S. Ashhab, and F. Nori, Quantum simulation, *Rev. Mod. Phys.* **86**, 153 (2014).

- [7] E. Manousakis, A quantum-dot array as model for copper-oxide superconductors: A dedicated quantum simulator for the many-fermion problem, *J. Low Temp. Phys.* **126**, 1501 (2002).
- [8] T. Byrnes, N. Y. Kim, K. Kusudo, and Y. Yamamoto, Quantum simulation of Fermi-Hubbard models in semiconductor quantum-dot arrays, *Phys. Rev. B* **78**, 075320 (2008).
- [9] T. Hensgens, T. Fujita, L. Janssen, X. Li, C. J. Van Diepen, C. Reichl, W. Wegscheider, S. Das Sarma, and L. M. K. Vandersypen, Quantum simulation of a Fermi-Hubbard model using a semiconductor quantum dot array, *Nature (London)* **548**, 70 (2017).
- [10] J. P. Dehollain, U. Mukhopadhyay, V. P. Michal, Y. Wang, B. Wunsch, C. Reichl, W. Wegscheider, M. S. Rudner, E. Demler, and L. M. K. Vandersypen, Nagaoka ferromagnetism observed in a quantum dot plaquette, *Nature (London)* **579**, 528 (2020).
- [11] C. J. van Diepen, T.-K. Hsiao, U. Mukhopadhyay, C. Reichl, W. Wegscheider, and L. M. K. Vandersypen, Quantum Simulation of Antiferromagnetic Heisenberg Chain with Gate-Defined Quantum Dots, *Phys. Rev. X* **11**, 041025 (2021).
- [12] R. Li, L. Petit, D. P. Franke, J. P. Dehollain, J. Helsen, M. Steudtner, N. K. Thomas, Z. R. Yoscovits, K. J. Singh, S. Wehner *et al.*, A crossbar network for silicon quantum dot qubits, *Sci. Adv.* **4**, eaar3960 (2018).
- [13] W. G. van der Wiel, S. De Franceschi, J. M. Elzerman, T. Fujisawa, S. Tarucha, and L. P. Kouwenhoven, Electron transport through double quantum dots, *Rev. Mod. Phys.* **75**, 1 (2002).
- [14] M. D. Shulman, O. E. Dial, S. P. Harvey, H. Bluhm, V. Umansky, and A. Yacoby, Demonstration of entanglement of electrostatically coupled singlet-triplet qubits, *Science* **336**, 202 (2012).
- [15] D. M. Zajac, T. M. Hazard, X. Mi, E. Nielsen, and J. R. Petta, Scalable Gate Architecture for a One-Dimensional Array of Semiconductor Spin Qubits, *Phys. Rev. Appl.* **6**, 054013 (2016).
- [16] S. F. Neyens, E. R. MacQuarrie, J. P. Dodson, J. Corrigan, N. Holman, B. Thorggrimsson, M. Palma, T. McJunkin, L. F. Edge, M. Friesen, S. N. Coppersmith, and M. A. Eriksson, Measurements of Capacitive Coupling Within a Quadruple-Quantum-Dot Array, *Phys. Rev. Appl.* **12**, 064049 (2019).
- [17] C. J. van Diepen, T.-K. Hsiao, U. Mukhopadhyay, C. Reichl, W. Wegscheider, and L. M. K. Vandersypen, Electron cascade for distant spin readout, *Nat. Commun.* **12**, 77 (2021).
- [18] C. Volk, A. M. J. Zwerver, U. Mukhopadhyay, P. T. Eendebak, C. J. van Diepen, J. P. Dehollain, T. Hensgens, T. Fujita, C. Reichl, W. Wegscheider, and L. M. K. Vandersypen, Loading a quantum-dot based “Qubyte” register, *npj Quantum Inf.* **5**, 29 (2019).
- [19] A. R. Mills, D. M. Zajac, M. J. Gullans, F. J. Schupp, T. M. Hazard, and J. R. Petta, Shuttling a single charge across a one-dimensional array of silicon quantum dots, *Nat. Commun.* **10**, 1063 (2019).
- [20] T.-K. Hsiao, C. J. van Diepen, U. Mukhopadhyay, C. Reichl, W. Wegscheider, and L. M. K. Vandersypen, Efficient Orthogonal Control of Tunnel Couplings in a Quantum Dot Array, *Phys. Rev. Appl.* **13**, 054018 (2020).
- [21] H. Qiao, Y. P. Kandel, K. Deng, S. Fallahi, G. C. Gardner, M. J. Manfra, E. Barnes, and J. M. Nichol, Coherent Multispin Exchange Coupling in a Quantum-Dot Spin Chain, *Phys. Rev. X* **10**, 031006 (2020).
- [22] J. Argüello-Luengo, A. González-Tudela, T. Shi, P. Zoller, and J. I. Cirac, Analogue quantum chemistry simulation, *Nature (London)* **574**, 215 (2019).
- [23] R. Loudon, One-dimensional hydrogen atom, *Proc. R. Soc. A* **472**, 20150534 (2016).
- [24] P.-F. Loos, C. J. Ball, and P. M. W. Gill, Chemistry in one dimension, *Phys. Chem. Chem. Phys.* **17**, 3196 (2015).
- [25] M. Imada, A. Fujimori, and Y. Tokura, Metal-insulator transitions, *Rev. Mod. Phys.* **70**, 1039 (1998).
- [26] S. Yang, X. Wang, and S. Das Sarma, Generic Hubbard model description of semiconductor quantum-dot spin qubits, *Phys. Rev. B* **83**, 161301(R) (2011).
- [27] C. J. Van Diepen, P. T. Eendebak, B. T. Buijtdorp, U. Mukhopadhyay, T. Fujita, C. Reichl, W. Wegscheider, and L. M. K. Vandersypen, Automated tuning of inter-dot tunnel coupling in double quantum dots, *Appl. Phys. Lett.* **113**, 033101 (2018).
- [28] K. C. Nowack, M. Shafiei, M. Laforest, G. E. D. K. Prawiroatmodjo, L. R. Schreiber, C. Reichl, W. Wegscheider, and L. M. K. Vandersypen, Single-shot correlations and two-qubit gate of solid-state spins, *Science* **333**, 1269 (2011).
- [29] OpenCV, Open source computer vision library, 2015.
- [30] D. Segal, P. Král, and M. Shapiro, Shaping of detached image states above suspended nanowires, *Phys. Rev. B* **69**, 153405 (2004).
- [31] W. I. L. Lawrie, H. G. J. Eenink, N. W. Hendrickx, J. M. Boter, L. Petit, S. V. Amitonov, M. Lodari, B. Paquelet Wuetz, C. Volk, S. G. J. Philips *et al.*, Quantum dot arrays in silicon and germanium, *Appl. Phys. Lett.* **116**, 080501 (2020).
- [32] J. Argüello-Luengo, A. González-Tudela, T. Shi, P. Zoller, and J. I. Cirac, Quantum simulation of two-dimensional quantum chemistry in optical lattices, *Phys. Rev. Research* **2**, 042013(R) (2020).
- [33] P. Scarlino, J. H. Ungerer, D. J. van Woerkom, M. Mancini, P. Stano, C. Muller, A. J. Landig, J. V. Koski, C. Reichl, W. Wegscheider *et al.*, *In-situ* tuning of the electric dipole strength of a double dot charge qubit: Charge noise protection and ultra strong coupling, *arXiv:2104.03045* (2021).
- [34] B. Bertrand, H. Flentje, S. Takada, M. Yamamoto, S. Tarucha, A. Ludwig, A. D. Wieck, C. Bäuerle, and T. Meunier, Quantum Manipulation of Two-Electron Spin States in Isolated Double Quantum Dots, *Phys. Rev. Lett.* **115**, 096801 (2015).
- [35] J. C. Bayer, T. Wagner, E. P. Rugeramigabo, and R. J. Haug, Charge reconfiguration in isolated quantum dot arrays, *Ann. Phys. (Leipzig)* **531**, 1800393 (2019).
- [36] T. H. Oosterkamp, T. Fujisawa, W. G. V. D. Wiel, K. Ishibashi, R. V. Hijman, S. Tarucha, and L. P. Kouwenhoven, Microwave spectroscopy of a quantum-dot molecule, *Nature (London)* **395**, 873 (1998).
- [37] P. Pakkiam, A. V. Timofeev, M. G. House, M. R. Hogg, T. Kobayashi, M. Koch, S. Rogge, and M. Y. Simmons, Single-Shot Single-Gate rf Spin Readout in Silicon, *Phys. Rev. X* **8**, 041032 (2018).
- [38] M. Urdampilleta, D. J. Niegemann, E. Chanrion, B. Jadot, C. Spence, P. A. Mortemousque, C. Bäuerle, L. Hutin, B. Bertrand, S. Barraud *et al.*, Gate-based high fidelity spin readout in a CMOS device, *Nat. Nanotechnol.* **14**, 737 (2019).
- [39] A. West, B. Hensen, A. Jouan, T. Tanttu, C. H. Yang, A. Rossi, M. F. Gonzalez-Zalba, F. Hudson, A. Morello, D. J. Reilly

- et al.*, Gate-based single-shot readout of spins in silicon, *Nat. Nanotechnol.* **14**, 437 (2019).
- [40] G. Zheng, N. Samkharadze, M. L. Noordam, N. Kalhor, D. Brousse, A. Sammak, G. Scappucci, and L. M. K. Vandersypen, Rapid gate-based spin read-out in silicon using an on-chip resonator, *Nat. Nanotechnol.* **14**, 742 (2019).
- [41] D. D. Vu and S. Das Sarma, One-dimensional few-electron effective Wigner crystal in quantum and classical regimes, *Phys. Rev. B* **101**, 125113 (2020).
- [42] D. D. Vu and S. Das Sarma, Collective ground states in small lattices of coupled quantum dots, *Phys. Rev. Research* **2**, 023060 (2020).
- [43] E. Townsend, T. Neuman, A. Debrecht, J. Aizpurua, and G. W. Bryant, Many-body physics in small systems: Observing the onset and saturation of correlation in linear atomic chains, *Phys. Rev. B* **103**, 195429 (2021).
- [44] A. Biborski, M. P. Nowak, and M. Zegrodnik, Correlation-induced *d*-wave pairing in a quantum dot square lattice, *Phys. Rev. B* **104**, 245430 (2021).
- [45] S. Manzeli, D. Ovchinnikov, D. Pasquier, O. V. Yazyev, and A. Kis, 2D transition metal dichalcogenides, *Nat. Rev. Mater* **2**, 17033 (2017).
- [46] X.-X. Song, D. Liu, V. Mosallanejad, J. You, T.-Y. Han, D.-T. Chen, H.-O. Li, G. Cao, M. Xiao, G.-C. Guo *et al.*, A gate defined quantum dot on the two-dimensional transition metal dichalcogenide semiconductor WSe<sub>2</sub>, *Nanoscale* **7**, 16867 (2015).
- [47] Z. Peng, X. Chen, Y. Fan, D. J. Srolovitz, and D. Lei, Strain engineering of 2D semiconductors and graphene: from strain fields to band-structure tuning and photonic applications, *Light Sci. Appl.* **9**, 190 (2020).
- [48] J. Knörzer, C. J. van Diepen, T.-K. Hsiao, G. Giedke, U. Mukhopadhyay, C. Reichl, W. Wegscheider, J. I. Cirac, and L. M. K. Vandersypen, Research Data for “Long-range electron-electron interactions in quantum dot systems and applications in quantum chemistry”, <https://doi.org/10.5281/zenodo.6035943> (2022).